IEEE Access
Multidisciplinary ⋮ Rapid Review ⋮ Open Access Journal

Received December 23, 2020, accepted January 8, 2021, date of publication January 13, 2021, date of current version January 22, 2021.

Digital Object Identifier 10.1109/ACCESS.2021.3051560

Efficient Image Reconstruction Algorithm for ECT System Using Local Ensemble Transform Kalman Filter

WAEL DEABES[1,2] **AND KHEIR EDDINE BOUAZZA**[1,3]

[1]Department of Computer Science in Jamoum, Umm Al-Qura University, Makkah 25371, Saudi Arabia
[2]Computers and Systems Engineering Department, College of Engineering, Mansoura University, Mansoura 35516, Egypt
[3]Laboratoire d'Informatique et des Technologies de l'Information d'Oran (LITIO), University of Oran, Oran 31000, Algeria

Corresponding author: Wael Deabes (wadeabes@uqu.edu.sa)

This work was supported by the National Plan for Science, Technology, and Innovation (MAARIFAH), King Abdulaziz City for Science and and Technology, Saudi Arabia under Grant 13-ELE469-10.

ABSTRACT One of the vital processes that should be monitored and analyzed continuously in the oil-gas and petroleum-related industries is the multi-phase flow inside pipes. Multi-phase flow means flowing two or more phases of gas, liquid, or solid inside a pipe. Electrical Capacitance Tomography (ECT) is a feasible and economical solution for monitoring dynamic applications. The ECT system offers the benefits of no radiation, non-intrusive, and non-invasive. Despite its potential, ECT systems deployment's major limitation is the crucial need to develop rapid image reconstruction algorithms. In this paper, a Local Ensemble Transform Kalman Filter (LETKF) is developed as a non-linear system estimator for reconstructing images in the ECT system. This method manages each node of the model independently by assimilating only the observations at a predefined distance. The localized approach of the LETKF gives it high computational efficiency allowing it to be applied to large dynamic systems. A quantitative analysis using Image Error (IE) and Coefficient Correlation (CC) measures has been applied to prove the effectiveness of the proposed algorithm. Indeed, the IE has been significantly decreased (around 62%), and the CC greatly increased (around 58%). Then, the influence of the noise was discussed. The results are promising and prove the algorithm feasibility.

INDEX TERMS ECT, image reconstruction, Kalman filter, multi-phase flow.

I. INTRODUCTION

Recently, the level of interest in the multi-phase flow measurements used in the oil-gas and petroleum-related industries is rapidly growing. The multi-phase flow is a movement of some materials inside a pipe such as gas or solid in liquid [1]–[4]. According to the process conditions, there is a distinct need to know the multi-phase flow parameters such as mass, velocity to increase effectiveness, quality, and decreasing processing expenses. In Particular, petrochemical companies in Saudi Arabia are mainly interested in knowing the flow types (annular, stratified, bubble flows, etc.) at a particular time of their process [5], [6]. It is essential to state that the visualization process is an exciting measurement process and has recently achieved substantial advances in hardware and software technologies [7], [8].

The associate editor coordinating the review of this manuscript and approving it for publication was Qiangqiang Yuan.

Visualization techniques of computed tomography span a wide range of sensing modalities. Some interesting techniques are Ultrasound Tomography (UT), and Optical Coherence Tomography (OCT). In fact, UT technique, sensitive to variations in the acoustic impedance of objects, has been used for the detection of the multi-phase flow [9]–[11]. In [12], the principle and technical realization of OCT technique are explained.

This research will focus on electrical tomography methods [13], [14]. The electrical tomography systems, such as the Electrical Resistivity Tomography (ERT) [15], [16], Magnetic Induction Tomography (MIT) [17]–[19], and Electrical Capacitance Tomography (ECT) [20]–[24] are interesting. These modalities are real-time imaging, safe, suitable for different vessel sizes, and inexpensive. ECT technology, as a non-subversive and non-parasitic well-established imaging method, is capable of inducing a cross-sectional image representing the inner distribution of permittivity based on outer

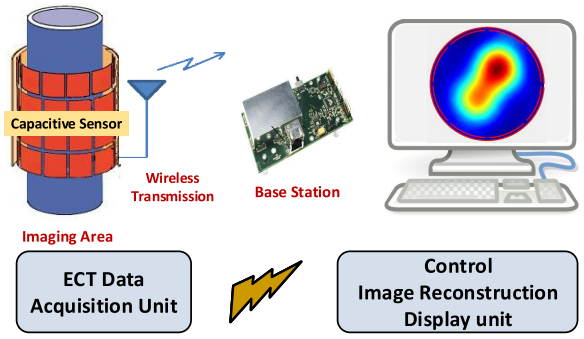

FIGURE 1. The ECT system components.

capacitance measurements. Typically, the basic components of the ECT system are an array of capacitance sensors, a data acquisition system, and a computer for building and displaying images. Fig. 1 shows these main components of the ECT system [25]. The electrical tomography process usually starts by collecting the data from the sensors, reconstructs the distribution images, and displays the results [26].

The ECT sensor is composed of multiple exciting electrodes, which are evenly mounted around the non-conductive dielectric medium of the material inside the vessel to be imaged. There is an earthed screen positioned outside the electrodes to depress the exterior interference noise to accomplish such a process. The functioning of the ECT system depends on gauging the change in capacitance measurement of a multi-electrode ECT sensor. This process is carried out by the variations in the distribution and/or condensation of dielectric materials inside the vessels. The outcome is the reconstruction of cross-sectional images representing the permittivity distribution obtained from the measured data [27].

There are two computational problems associated with the tomography system, forward and inverse problems. Forward problem solves partial differential equations governing the sensing domain, usually using Finite Element Methods (FEM) to calculate the capacitance measurements. While the inverse problem generates distribution images from known capacitance measurements using image reconstruction algorithms [8]. The image pixels' number (Unknown) is larger than the measurement number (Known); therefore, the inverse problem is ill-posed. Another challenge is that the nonlinear relationship between material distribution and the measurements [28].

To obtain more accurate and sharper images of the materials distribution, iterative image reconstruction algorithms are crucial [29], [30]. In the iterative techniques, the inverse and forward problems are solved in a continuous loop until an acceptable measurement error rate is reached. The Iterative Linear Back Projection (ILBP) is a standard procedure for building the images [31], [32]. Nevertheless, when a sharp transition exists between the different materials, the obtained images are blurred and suffer from a smoothing effect.

The image reconstruction techniques used in the electrical tomography can be classified into Algebraic Reconstruction Techniques (ART) and Optimization Reconstruction Techniques (ORT) [25], [33]. In the first class, the system responses to density variations in the imaging domain can be modeled as a set of algebraic equations. Next, a sensitivity map describing the tomography sensor response is generated using the measured signal. Afterward, the set of independent equations is solved based on matrix manipulation. While in optimization techniques, a set of objective functions are optimized to obtain the most expected image associated with the measured signal. Usually, the nonlinearity level between the detected signal and the density distribution dramatically affects each reconstruction approach's performance when applied to different tomography modalities. For instance, ECT and ERT are two electrical tomography techniques where the density distribution is non-linearly related to the electric field distribution inside the imaging domain. The optimization techniques in these two examples provide better imaging results compared to algebraic techniques.

One of the main challenges of this research is the extreme nonlinear response of the tomography system. Therefore, building a precise and fast algorithm for creating the images and overcome these limitations is essential. Iterative algorithms, compared to non-iterative algorithms, are more significant in avoiding the nonlinearity problem and building more detailed images [34]. However, the time required for the iterative ones is longer since it regularly needs two steps to solve the forward and inverse problems. The implementation of most iterative methods requires high computations since these algorithms are based on complex mathematical models and run iteratively to obtain the best image. Therefore, we introduce an efficient Local Ensemble Transform Kalman Filter (LETKF) to estimate the dynamic multi-phase flow using ECT system with high accuracy and considerably reduces the computation time.

After recalling the components of the ECT system in section II and how the sensitivity analysis is carried out, the different theoretical and practical steps that led to the development of the LETKF algorithm are presented and explained in section III. Numerical results presented in section IV show good performances achieved by applying the proposed LETKF algorithm. The final section V concludes the proposed work.

II. ELECTRICAL CAPACITANCE TOMOGRAPHY (ECT)

Typically, a capacitance sensor, a data acquisition system, and a computer system are three main components formed the ECT system [35]. The distribution of an array of electrodes around the vessel required to be imaged is shown in Fig. 2a. The outside earthed screen filters any external noises and disturbances. Consecutively, all independent capacitive measurements are captured by firing one electrode to work as transmitter, and the rest of the electrodes as receivers in the ECT sensor [36]. The measurements' change is proportional to the permittivity change inside the imaging area.

Reconstructing the ECT images involves solving forward and inverse problems [2]. Equation 1 solves the forward problem by estimating the electrical response u corresponding to

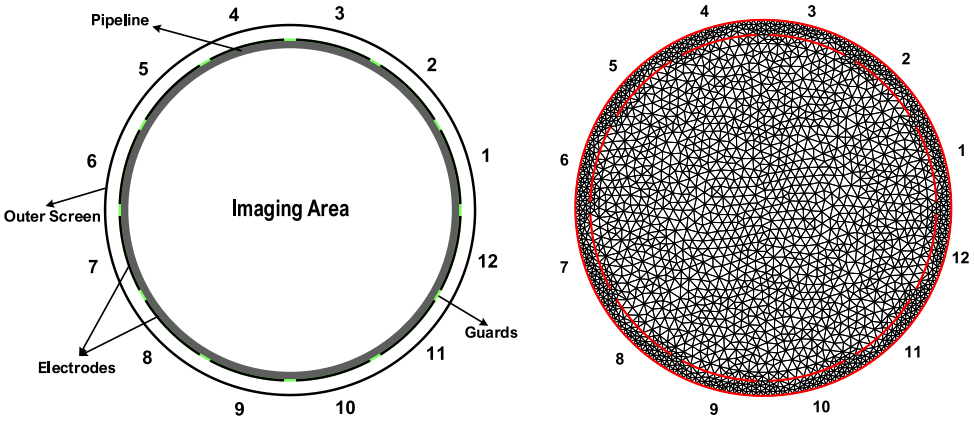

(a) ECT sensor (b) Finite Element Model

FIGURE 2. ECT system with 12 electrodes.

known permittivity distribution ε, and the boundary electrical potential.

$$\begin{aligned} \nabla \cdot (\varepsilon \nabla u) &= 0 \text{ on } \Omega \\ u &= b \text{ on } \Omega \end{aligned} \tag{1}$$

where Ω is the imaging area, and b is the electric potential.

The capacitance measurements are calculated in the forward problem with respect to each pixel's perturbation in the imaging area from the low permittivity value to the high value to compute the jacobian. The jacobin is called the sensitivity matrix S, which is applied in the solution of the inverse problem to reconstruct the corresponding image as shown in Eq. 2:

$$G = S^T \cdot C \tag{2}$$

where G is the permittivity distribution, and C is the capacitance [37].

Finite Element Model (FEM) is applied to model the forward problem in the ECT system and calculate the sensitivity matrix [38]. Fig. 2b represents the FEM with 4112 nodes for ECT sensor consisting of 12 electrodes. The sensitivity matrix is calculated according to Eq. 3:

$$S_i = \frac{C_i^F - C_i^j}{C_i^F - C_i^E} \quad (j = 1, 2, \ldots, e) \tag{3}$$

where $S_i (i = 1, 2, \ldots, 66)$ represents the sensitivity matrix for electrode pair i, e is the number of nodes, C^F is the measurements vector when all nodes have high permittivity value, C^j are measurements when just node j assigned high permittivity value, C^E are the measurements when the nodes have the low permittivity value. Fig. 3 shows the different sensitivity matrix between electrodes 1-3, 1-5, and 1-7.

III. TIME-VARYING MODEL

We suppose that the time-based estimation of the materials distribution x_k is linear over the domain ω:

$$x_{k+1} = B_k x_k + z_k \tag{4}$$

where B_k is the state transition matrix at time t_k. Without loss of generality, we suppose that $B_k = I$ (i.e. identity matrix) for all $t_k (k = 1, 2, 3, \ldots)$, z_k is represented as a white Gaussian noise and its covariance matrix $\Gamma_k^z \equiv E[z_k \; z_k^T]$. W_k represents the measurements produced by the kth applied voltage. The measurements are represented by a nonlinear relation with the error of the measurement:

$$W_k = U_k(x_k) + r_k \tag{5}$$

where r_k is a white Gaussian noise with the covariance matrix $\Gamma_k^r \equiv E[r_k \; r_k^T]$.

The linearization of equation (5) around the nominal value x_0 gives:

$$W_k = U_k(x_0) + J_k(x_0).(x_k - x_0) + H.O.Ts + r_k \tag{6}$$

where J_k is the Jacobian matrix defined by

$$J_k(x_0) = \left. \frac{\partial U_k}{\partial x_k} \right|_{x_k = x_0} \tag{7}$$

and H.O.Ts represent the higher order terms assumed to be additional white Gaussian noise. Let us define an artificial measurement (pseudo-measurement) by:

$$y_k \equiv W_k - U_k(x_0) + J_K(x_0) \cdot x_0 \tag{8}$$

then the linearization of the measurement equation gives:

$$y_k = J_k(x_0).x_k + \bar{w}_K \tag{9}$$

where $\bar{w}_k$ represents the measurement and linearization errors with the known covariance matrix $\bar{\Gamma}_k^v = E[\bar{w}_k \; \bar{w}_k^T]$.

A. INVERSE PROBLEM SOLVER BASED ON Extended Kalman Filter (EKF)

The use of Kalman filter allow us to estimate the vector x_k using the precedent measurements taken up to t_k. The

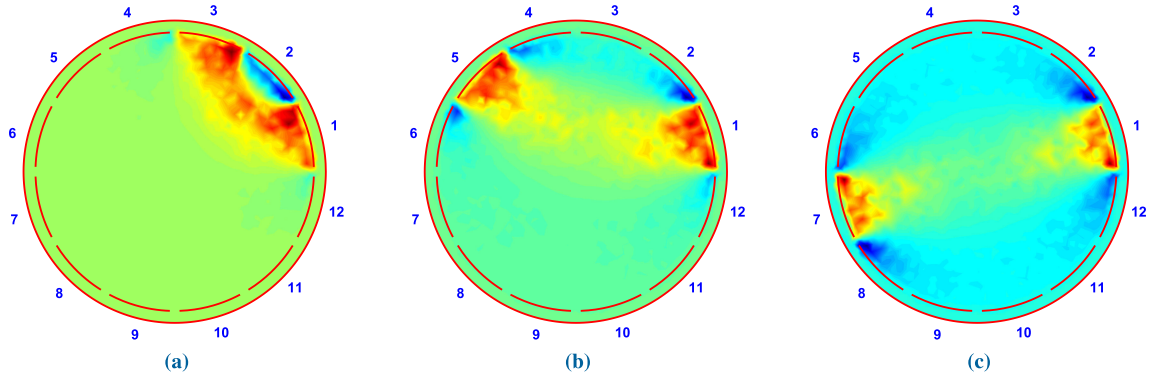

FIGURE 3. Sensitivity patterns for electrode separation by 1, 3, and 5 electrodes.

estimation is performed by minimizing the following cost functional:

$$\Xi(x_k) = \frac{1}{2}\left\{\|x_k - x_{k|k-1}\|^2_{c^{-1}_{k|k-1}} + \|y_k - J_k(x_0)\|^2_{\Gamma_k^{-1}}\right\} + \left\{\beta \left\|V(x_k - x^*)\right\|^2\right\} \quad (10)$$

where β and V denotes the regularization parameter and the regularization matrix, respectively, x^* is the previous data and $R_{k|k-1}$ represents the error covariance matrix given as:

$$R_{k|k-1} = E\left[(x_k - x_{k|k-1})(x_k - x_{k|k-1})^T\right] \quad (11)$$

The augmented pseudo-measurement and Jacobian matrices are given by:

$$\bar{y}_k = \begin{bmatrix} y_k \\ \sqrt{\beta}\cdot V \cdot x^* \end{bmatrix} \quad (12)$$

$$H_k = \begin{bmatrix} J_k(x_0) \\ \sqrt{\beta}\cdot V \end{bmatrix} \quad (13)$$

Then we can rewrite the precedent cost functional as:

$$\Xi(x_k) = \frac{1}{2}\left\{\|x_k - x_{k|k-1}\|^2_{R^{-1}_{k|k-1}} + \|\bar{y}_k - H_k . x_k)\|^2_{\Gamma_k^{-1}}\right\} \quad (14)$$

where Γ_k is the following block diagonal matrix

$$\Gamma_k \equiv Blockdiag\left[\bar{\Gamma}^v_k,\ I\right] \quad (15)$$

Then, the recursive EKF obtained by minimizing the cost functional (equation (10)) consists of two steps [39]:

Step 1. Correction Filter:

$$L_k = R_{k|k-1}\, H_k^T \left[H_k\, R_{k|k-1}\, H_k^T + \Gamma_k\right]^{-1} \quad (16)$$

$$R_{k|k} = [I_N\ - L_k\, H_k]\, R_{k|k-1} \quad (17)$$

$$x_{k|k} = x_{k|k-1} + L_k\left[\bar{y}_k - H_k x_{k|k-1}\right] \quad (18)$$

Step 2. Prediction Process:

$$R_{k+1|k} = B_k R_{k|k} B_k^T + \Gamma_k^w \quad (19)$$

$$x_{k+1|k} = B_k x_{k|k} \quad (20)$$

However, the use of EKF may not meet users' expectations, especially when dealing with large-scale dynamics or real-time implementation. Indeed, storage and computation time requirements arise quickly when using an EKF on a real-time or high dimensional system. Considering a model with a state vector composed of m unknowns, then the error covariance matrix R_k will have m^2 unknowns. For large systems or real-time implementation, computing and updating the error covariance matrix will require a very high computational cost. As a result, EKF is not suitable for this kind of system. Therefore, it is necessary for real-time or high dimensional problems to find a better way to update the covariance equation.

B. ENSEMBLE KALMAN FILTER (EnKF)

This section aims to allow Kalman filtering, performed in real-time, on large dimension dynamic systems. The main idea that led to the Ensemble Kalman Filter (EnKF) is to provide an estimator that can be applied to large scale systems. In the EnKF, ensemble statistics are used to predict and analyze the covariance matrix (R_k).

G. Evensen introduced the EnKF in 1994 [40] in order to deal with large-scale ocean models. Subsequently, the EnKF has been further developed for different applications in several articles. The different EnKF development stages can be found and explained in [41]. Other important and promising results have come to show the interest of EnKF, we can cite its application to the marine ecosystem presented by M. Eknes and G. Evensen [42] and J. I. Allen et. Al. [43]. Recently, the EnKF properties have shown exciting results in oil reservoirs modeling. In this section, the theoretical formulas of the EnKF will be presented. Further details on the EnKF can be found in Evensen's book [44].

1) EnKF ALGORITHM

The algorithm of the EnKF is as follows [41].

a. The initial estimation

- Generate the N-ensembles of the initial estimation

$$\hat{x}_{1,i} = [\hat{x}_{1,1}\ \hat{x}_{1,2}\ \hat{x}_{1,3}\ \ldots\ \hat{x}_{1,n}] \text{ with } \hat{x}_{1,i} \sim N(x_1^-, P_1)$$

- Compute mean of the initial estimation

$$\hat{x}_1 = \frac{1}{n}\sum_{i=1}^{N}\hat{x}_{1,i} \tag{21}$$

b. The prediction step

- Generate N-ensemble for the state variable in the prediction step as follows

$$\hat{x}^-_{k+1,i} = B_k\hat{x}_{k,i} + \varsigma_{k,i} \tag{22}$$

with $\varsigma_{k,i} \sim N(1, Q_k^{\Gamma})$ is the ensemble of the noise system.

- Mean of prediction step estimation

$$\hat{x}^-_{k+1} = \frac{1}{n}\sum_{i=1}^{N}\hat{x}^-_{k+1,i} \tag{23}$$

- Compute Error covariance of the prediction step estimation

$$R^-_{k+1} = \frac{1}{N-1}\sum_{i=1}^{N}\left(\hat{x}^-_{k+1,i} - \hat{x}^-_{k+1}\right)\left(\hat{x}^-_{k+1,i} - \hat{x}^-_{k+1}\right)^T \tag{24}$$

c. The correction step

- Generate the ensemble of the measurement data

$$\bar{y}_{k+1,i} = \bar{y}_{k+1} + \zeta_{k,i} \tag{25}$$

with $\zeta_{k,i} \sim N(1, Rk^{\Gamma})$ is the ensemble of measurement noise.

- Kalman gain is then defined as

$$L_k = R^-_{k+1}H_k^T\left(H_kR^-_{k+1} + \Gamma_k\right)^{-1} \tag{26}$$

- Estimation of the correction step is

$$\hat{x}_{k+1,i} = \hat{x}^-_{k+1,i} + L_k\left(\bar{y}_{k+1,i} - H_k\hat{x}^-_{k+1,i}\right) \tag{27}$$

- Mean of the correction step estimation

$$\hat{x}_{k+1} = \frac{1}{N}\sum_{i=1}^{N}\hat{x}_{k+1,i} \tag{28}$$

with the error covariance

$$R_{k+1} = [1 - L_kH_k]\,R^-_{k+1} \tag{29}$$

d. Substitute (28) into the prediction step (22).

e. Repeat and continue step (b) and step (c) until we get mean of the correction step estimation as the result of estimation.

2) CHALLENGES WITH THE EnKF

The EnKF schemes provide a computational methodology for the computation and propagation of a flux-dependent predictive covariance matrix, R^-_{k-1}. Unfortunately, R^-_{k-1} is of rank $k-1$ at most, and can therefore only take into account the estimation uncertainty in at most $k-1$ directions.

Indeed, computational limitations limit the ensemble size to be much smaller than the state size, which leads to a very serious rank-deficiency approximation of the actual covariance matrix of the estimated global state. This rank of deficiency can cause a poor analysis quality due to sampling errors. Due to practical limitations, a larger ensemble may not be an option; therefore, we must look to other approaches to correct the sampling errors.

C. LOCALIZED ESTIMATION

1) COVARIANCE LOCALIZATION

Covariance localization allows removing the correlations between the model variables whose spatial distance exceeds a certain prescribed distance from a given node. The update state at that node will depend only on observations and model variables inside a finite distance. This is a desirable approach because the nearby observations and model variables have a stronger correlation with the quantities defined at the given node because their covariance is best represented with a reasonably sized ensemble. Localization helps avoid the influence of distant observations, which, although not having physically significant correlations with the given node, can have spurious correlations resulting from sampling errors of the undersized ensemble. A too-small localization radius can degrade the analysis, as it can remove correlations that are physically and temporally significant and, therefore, beneficial for the analysis accuracy. A small localization radius can also cause imbalances or unwanted small-scale noise into the analysis.

To avoid these adverse effects, the typical approach is to multiply the EnKF estimated error sample covariances by a weighting factor that will gradually decrease until it reaches zero at a finite distance. The influence of observations gradually decreases to zero. The localization radius should ideally be large enough to take account of physically significant correlations and small enough to exclude long distance spurious correlation.

2) COVARIANCE INFLATION

Suppose the EnKF is applied to large nonlinear models. In that case, the model covariance matrix may be several orders of magnitude larger than the ensemble size, which does not allow the ensemble to represent the global model dynamics statistically and will probably distort long-range correlations.

By applying covariance localization, the sampling errors can be compensated, but the ensemble may locally distort the model covariance in some regions due to nonlinearities in the model. Covariance inflation has the advantage of being

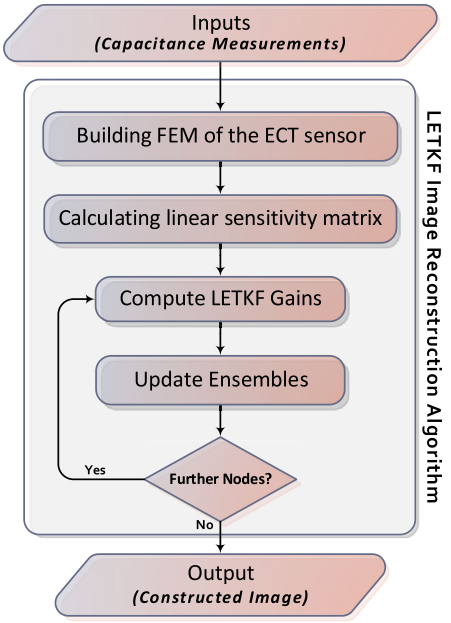

FIGURE 4. The flow chart of the LETKF algorithm.

an ad hoc approach that compensates for these drawbacks. It consists of multiplying the disturbance matrix, X^b by a constant factor $\rho > 1$ to increase its ensemble spread, which reduces the confidence of the EnKF diagram on the model variable N-ensemble.

3) LOCAL ENSEMBLE TRANSFORM KALMAN FILTER (LETKF)

LETKF is a local ensemble square-root filter which transforms the ensembles at a fixed time, $\{x^{b(i)}\}$, $i = 1; 2; \ldots; K$ (K is the ensemble members number), into an analysis ensemble, $\{x^{a(i)}\}$, $i = 1; 2; \ldots; K$. This method handles each node independently, assimilating only the observations located within a defined distance, to obtain an ensemble of analyzed local state vectors as is described hereafter. Finally, we assemble the local analyzed ensembles to build a set of global analyzed states.

Each local analysis only considers the uncertainty of prediction at the local level, whose dimension is usually much less than the overall uncertainty. Therefore, the global analysis can be computed accurately by using only an ensemble of average size. The LETKF is a naturally parallel algorithm since each node is updated independently. Furthermore, the computation operations are based on the ensemble size and the number of observations and not the state size. Fig. 4 shows the flow chart of the proposed LETKF image reconstruction algorithm.

Let x be a state vector of the time variant dynamic model representing materials distribution. As initial conditions for generating the ensembles $x^{b(i)}$, $i = 1; 2; \ldots K$ (K is the ensemble members number), we use the analysis ensembles in the previous analysis step. Let X^b be the matrix whose columns contain the start from each ensemble $x^{b(i)}$ from the ensemble mean $\bar{x}^b$ where the i-th column of X^b is $x^{b(i)} - \bar{x}^b$. In order to transform the estimated state from the state space to the observation space, the observation operator H_k is applied to the ensemble $x^{b(i)}$, to obtain $y^{b(i)} = H(x^{b(i)})$. Consider $Y^b = y^{b(i)} - \bar{y}^b$ as the estimated disturbances in the observation space. Then, the basic information is ready to be compared with observations in the same space.

The LETKF assimilates only the observations at a certain distance from each node, in order to update the analysis states at each node. The index (l) is used to denote a quantity defined on such a local region centered on an analysis node. The analysis mean $\bar{x}^a_{(l)}$, is given by

$$\bar{x}^a_{(l)} = \bar{x}^b_{(l)} + X^b_{(l)}\bar{w}_{(l)} \tag{30}$$

where $\bar{w}_{(l)}$ is the mean weighting vector given by

$$\bar{w}_{(l)} = \tilde{P}^a_{(l)} \left(Y^b_{(l)}\right)^T R^{-1}_{(l)} \left(y^o_{(l)} - y^b_{(l)}\right) \tag{31}$$

where

$$\tilde{P}^a_{(l)} = \left[\left(Y^b_{(l)}\right)^T R^{-1}_{(l)} \left(Y^b_{(l)}\right) + (k-1)I/\rho\right]^{-1} \tag{32}$$

is the analysis error covariance in the ensemble space, R is the observation error covariance matrix, y^o is the observation vector, and ρ is the multiplicative inflation factor.

Inside a local region, spatial localization is performed by multiplying the inverse observation error covariance matrix by a factor that decreases from one to zero when the distance of the observations to the node of analysis increases.

Therefore, the ensemble perturbations of the analysis are given by

$$X^a_{(l)} = X^b_{(l)} \left[(K-1)\tilde{P}^a_{(l)}\right]^{1/2} \tag{33}$$

which estimates the uncertainty of the analysis and the global analysis ensemble $x^{a(i)}$ is deduced by gathering the values of $\bar{x}^a_{(l)}$ and $X^a_{(l)}$ at all nodes.

4) IMPLEMENTATION OF THE LETKF

In this section, we explain how the LETKF algorithm is implemented for reconstructing images for ECT systems.

IV. RESULTS AND DISCUSSION

A. SIMULATION EXPERIMENT (NOISE-FREE MEASUREMENTS)

Numerical simulations have been carried out to assess the practicability of the proposed algorithm. Typically, the oil-gas two-phase flow was simulated, and 3 typical flow patterns were tested. The relative permittivity of the oil and gas is set to 4 and 1, respectively. A Matlab software package using Gmesh FEM software is implemented to compute the solutions of the ECT's problems. The ECT consists of 12 electrodes and its FEM has 4112 nodes, as shown in Fig. 2. The radii of the outside screen and the pipe are 85mm, and 50mm, respectively. The thickness of the pipe wall equals 10mm. The dimensions of each electrode are 62.5 mm, 30 mm, and 1 mm.

Algorithm 1 LETKF

Input: Capacitance Measurements
Output: Reconstructed Image
/* Initialization */
Generate the ensembles $\{x^{b(i)}\}$
$\{y^{b(i)}\} \leftarrow H_k(\{x^{b(i)}\})$ // H_k is the nonlinear observation matrix
$Y^b(i) \leftarrow y^{b(i)} - \bar{y}^b$ // $\bar{y}^b$ the ensemble mean of $\{y^{b(i)}\}$
$X_b(i) \leftarrow x^{b(i)} - \bar{x}^b$ // $\bar{x}^b$ is the ensemble mean of $\{x^{b(i)}\}$
for $j = 1 : e$ **do** // e is the number of image nodes
    Update $\tilde{P}^a_{(l)}$ by (32)
    Update $X^a_{(l)}$ by (33)
    Update $\bar{w}_{(l)}$ by (31)
    Update $\bar{x}^a_{(l)}$ by (30)
Collect the results of Step 9 to form the global analysis ensemble $\{x^{a(i)}\}$

Several two-phase flow patterns as annular, core, bubble, and Stratified flows are simulated and illustrated in the 1^{st} column in Fig. 5. The circular bubbles in all the simulations have a radius equals to 15.85mm. The accuracy of the proposed image reconstruction algorithm LETKF is verified using different material distributions and compared with well-known algorithms such as Linear Back Projection (LBP) and Tikhonov algorithms.

To evaluate the image reconstruction algorithm quantitatively, the relative Image Error (IE) (Eq. (34) and Correlation Coefficient (CC) (Eq. 35) are applied.

$$IE = \frac{\|G^* - G\|}{\|G\|} \tag{34}$$

$$CC = \frac{\sum_{i=1}^{N}(G_i - \bar{G})(G_i^* - \bar{G^*})}{\sqrt{\sum_{i=1}^{N}(G_i - \bar{G})^2 \cdot \sum_{i=1}^{N}(G_i^* - \bar{G^*})^2}} \tag{35}$$

where G is the actual permittivity distribution of the test object, G^* is the reconstructed permittivity distribution, and $\bar{G}$ and $\bar{G^*}$ are the mean values of G and G^*, respectively.

The first column Fig. 5 represents the distribution of the real material, while the second, third, and fourth columns containing the reconstructed images from the LBP, Tikhonov, and LETKF algorithms, respectively. The Tikhonov iteration number is 200 iterations. The results of the LETKF algorithm have high quality and accuracy with sharp objects' boundaries compared with the reconstructed images from the LBP and Tikhonov algorithms. The number of ensemble members has been practically chosen equal to 25. Also, the covariance inflation factor ρ has been empirically selected to be equal to 1.25 for nodes located within a radius of 100 nodes; in the next 50 nodes, the value of ρ decreases linearly to 1.15; it decreases again until reaching 1.1 for the next 50 nodes, and is equal zero beyond the circle of radius of 200 nodes.

The LETKF algorithm is fast as well as the accuracy of its reconstructed images are high. The reconstruction time of the three algorithms are shown in Table 1. The Simulations are carried out using a PC with an i9 CPU (3.6 GHz) and 32 GB memory.

TABLE 1. Reconstruction time in sec.

LBP	Tikhonov	LETKF
0.026	5.3257	1.310

TABLE 2. IE for noise-free measurements.

Flow Phantom	LBP	Tikhonov	LETKF
Annular	0.3175	0.3631	0.1320
Core	0.6853	0.6562	0.2606
Two Objects	0.8641	0.6638	0.2585
Three Objects	0.9753	0.7492	0.2567
Stratified	0.7523	0.6953	0.2380

As shown in Eqs. (34) and (35), better reconstructed images should have smaller IE and larger CC. Tables 2, and 3 contain IE, and CC, respectively of the reconstructed images showed in Fig. 5. The proposed LETKF algorithm generates better images with low relative error and high correlation. The third phantom two objects are separated after applying the LETKF algorithm, while the results from LBP or Tikhonov algorithms have artifices. For instance, the IE index of the annular, and core flows have been improved by around 64%, 61%, respectively when compared to the Tikhonov algorithm. Also, the CC index of the annular, and three objects flows have been improved by around 14%, 58%, respectively when compared to the Tikhonov algorithm. The LETKF's a reconstructed image of the Stratified phantom is significantly enhanced and has better fidelity.

B. SIMULATION EXPERIMENT (NOISE-CONTAMINATED MEASUREMENTS)

The performance of the LETKF algorithm is tested by applying noise-contaminated simulated capacitance measurements with an SNR of 45dB. Fig. 6 represents the reconstructed

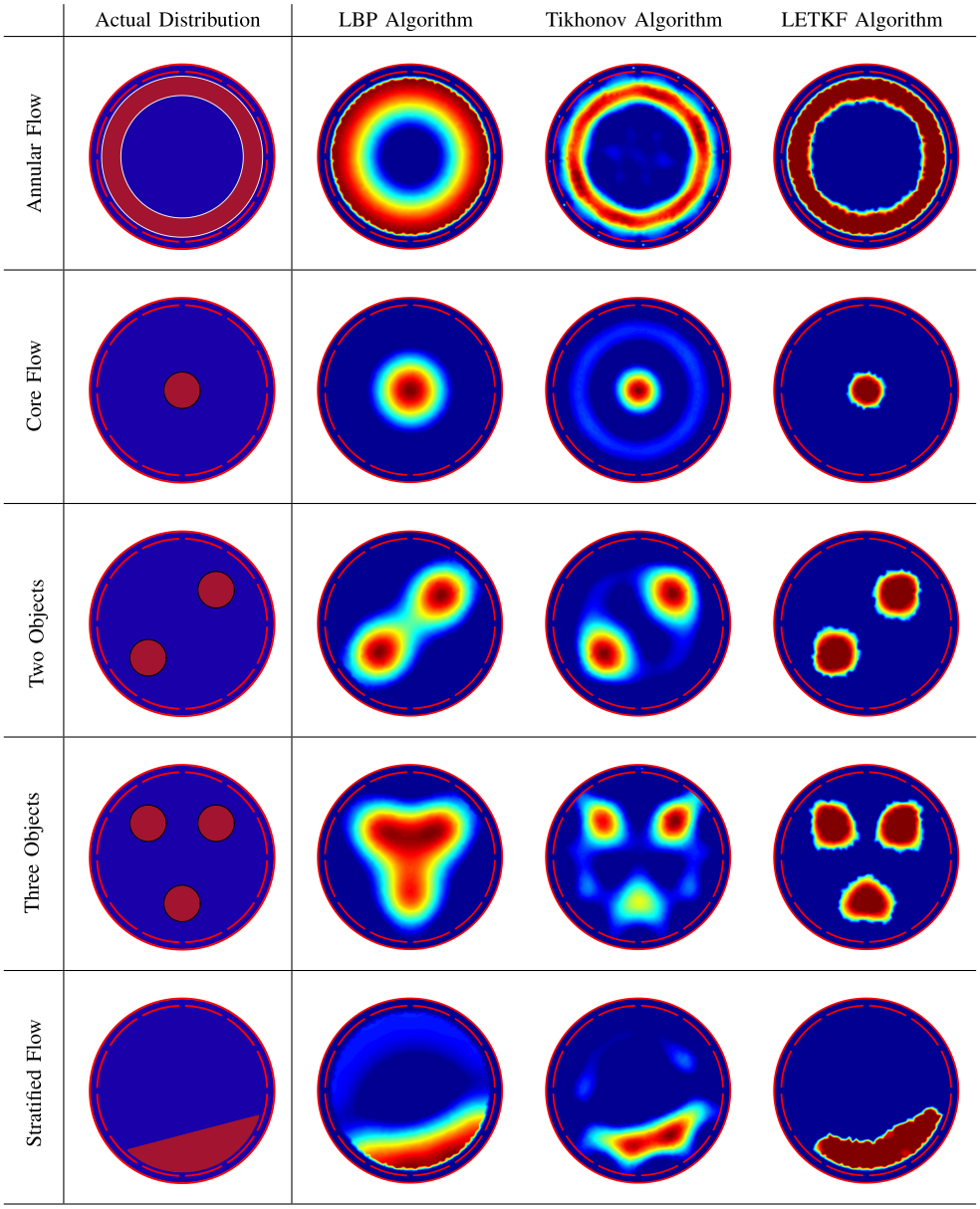

FIGURE 5. Reconstructed images of noise-free measurements.

TABLE 3. CC for noise-free measurements.

Flow Phantom	LBP	Tikhonov	LETKF
Annular	0.7486	0.8567	0.9756
Core	0.6785	0.7754	0.8481
Two Objects	0.5175	0.8565	0.8726
Three Objects	0.4185	0.5652	0.8943
Stratified	0.6454	0.4232	0.9144

TABLE 4. IE for noise-contaminated measurements.

Flow Phantom	LBP	Tikhonov	LETKF
Annular	0.3813	0.3740	0.2336
Core	0.6551	0.7142	0.1666
Two Objects	0.9263	0.4908	0.2499
Three Objects	0.9968	0.7552	0.2691
Stratified	0.6850	0.5706	0.3419

images from LBP, Tikhonov, and LETKF algorithms. The numerical values of the IE, and CC are stated in the Tables 4-5. The reconstructed images quality of the LBP and Tikhonov algorithms, shown in Fig. 6, is low compared with the reconstructed images from the LETKF algorithm.

C. IMAGE RECONSTRUCTION FROM EXPERIMENTAL DATA

The digital Electrical Capacitance Volume Tomography (ECVT) system developed by Tech4Imaging [45] is used to run the experiment. The ECVT has 36 channels, which can

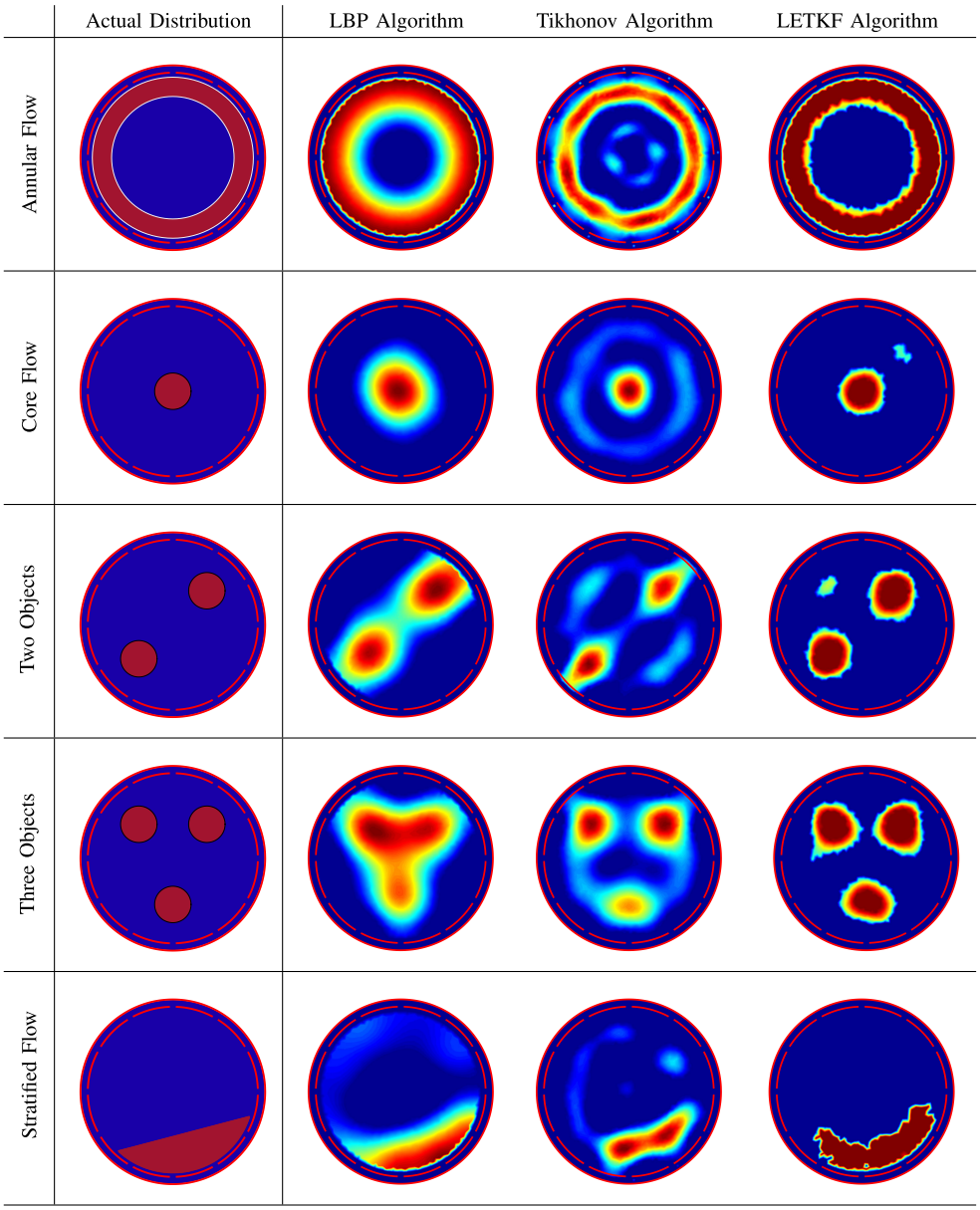

FIGURE 6. Reconstructed images of noise-contaminated measurements.

TABLE 5. CC for noise-contaminated measurements.

Flow Phantom	LBP	Tikhonov	LETKF
Annular	0.7436	0.8269	0.9158
Core	0.6125	0.6501	0.9280
Two Objects	0.3586	0.8035	0.8806
Three Objects	0.4214	0.6548	0.8834
Stratified	0.5365	0.4452	0.8241

measure the capacitance between 3 levels of 12 electrodes each. The system can generate 120 images/s.

The experiment is carried out by placing static phantoms in an imaging area with a radius of 63mm and measuring the capacitance of the 12 electrodes in the lower level. The stratified flow is tested by placing a plastic plate to split the pipe into two sections. One section is filled with plastic particles ($\epsilon = 3.6$). Two plastic rods ($r = 8mm$) were placed inside the imaging area to experiment with the bubble flow.

Fig. 7 demonstrates the real distributions and the generated images from LBP, Tikhonov, and LETKF algorithms. The created images from the LETKF algorithm have high accuracy and particular boundaries between the empty and filled sections compared with the other two algorithms. Also, the LETKF reconstructed two rods and annular distribution images have fewer artifacts. Tables 6, and 7 contain IE, and CC, respectively of the reconstructed images of real experimental setup shown in Fig. 7.

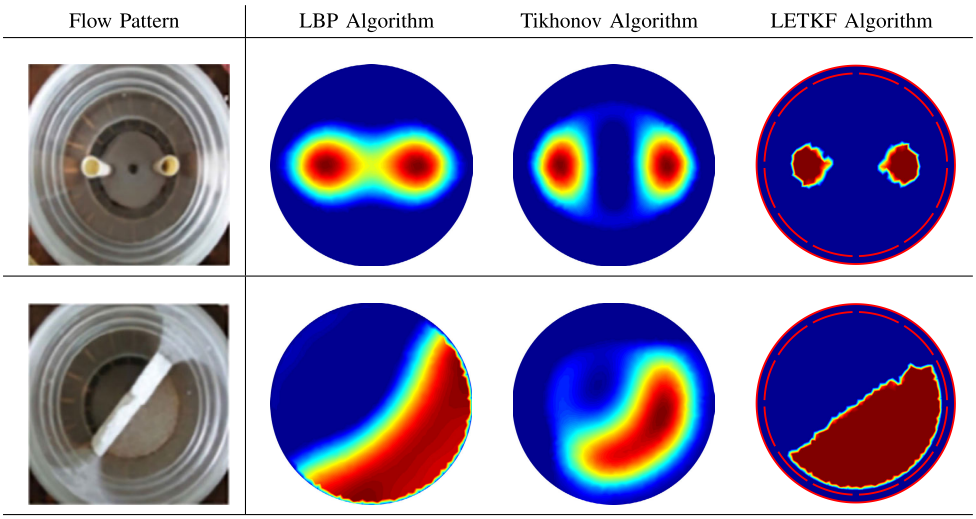

FIGURE 7. Experimental setup and reconstructed frames.

TABLE 6. IE for experimental measurements.

Flow Phantom	LBP	Tikhonov	LETKF
Two Objects	0.7742	0.6317	0.2135
Stratified	0.3125	0.3958	0.1130

TABLE 7. CC for experimental measurements.

Flow Phantom	LBP	Tikhonov	LETKF
Two Objects	0.6530	0.7157	0.9463
Stratified	0.7481	0.7052	0.9773

V. CONCLUSION

In this work, LETKF algorithm for reconstructing the images in the ECT is introduced. The proposed algorithm overcomes the nonlinearity constraints associated with the ECT systems. The inputs and outputs of the LETKF are the measured capacitance values, and material permittivity value in each node, respectively. Its localized approach allows LETKF to overcome the challenges encountered in previous Kalman filtering schemes, as well as to have high computational efficiency allowing it to be applied to large dynamic systems. Matlab implementations were carried out to solve the forward and inverse problems. The results demonstrate the feasibility of the proposed LETKF algorithm to reconstruct the material distribution inside the imaging area.

LIST OF NOMENCLATURE AND ABBREVIATION

UT Ultrasound Tomography
OCT Optical Coherence Tomography
ECT Electrical Capacitance Tomography
ERT Electrical Resistivity Tomography
MIT Magnetic Induction Tomography
ILBP Iterative Linear Back Projection
ART Algebraic Reconstruction Techniques
ORT Optimization Reconstruction Techniques
FEM Finite Element Model
EKF Extended Kalman Filter
EnKF Ensemble Kalman Filter
LBP Linear Back Projection
IE Image Error
CC Correlation Coefficient
ECVT Electrical Capacitance Volume Tomography
LETKF Local Ensemble Transform Kalman Filter

LIST OF SYMBOLS

ELECTRICAL CAPACITANCE TOMOGRAPHY

G Permittivity distribution
C Capacitance measurements
S Sensitivity matrix
Ω Imaging area
b Electric potential

KALMAN FILTER

B_k State transition matrix
x_k State vector representing the material distribution
W_k Measurements vector
z_k White Gaussian noise
y_k Pseudo measurement vector
Γ_k^z State error covariance Matrix
Γ_k^r Measurement covariance matrix
J_k Jacobian Matrix
β Regularization parameter
V Regularization matrix
H_k Nonlinear observation matrix
R_k Observation error covariance matrix
L_k Kalman filter gain

ENSEMBLE KF

N number of ensembles
$\hat{x}$ State estimation vector

LOCAL ENSEMBLE TRANSFORM KF

K	Ensemble members number
x^a	State analysis ensemble
x^b	Estimated State ensemble
y^a	Observation analysis ensemble
y^b	Estimated observation ensemble
$\hat{x}^b$	Ensemble mean of $x^{b(i)}$
$\hat{y}^b$	Ensemble mean of $y^{b(i)}$
$\tilde{P^a}$	Analysis error covariance matrix
ρ	Multiplicative inflation factor
e	Number of image nodes

ACKNOWLEDGMENT

The authors would like to thank the King Abdulaziz City for Science and Technology for continuous support.

REFERENCES

[1] J. Yao and M. Takei, "Application of process tomography to multiphase flow measurement in industrial and biomedical fields: A review," *IEEE Sensors J.*, vol. 17, no. 24, pp. 8196–8205, Dec. 2017.

[2] E. J. Mohamad, R. A. Rahim, M. H. F. Rahiman, H. L. M. Ameran, S. Z. M. Muji, and O. M. F. Marwah, "Measurement and analysis of water/oil multiphase flow using electrical capacitance tomography sensor," *Flow Meas. Instrum.*, vol. 47, pp. 62–70, Mar. 2016.

[3] C. E. Agu, A. Ugwu, C. Pfeifer, M. Eikeland, L.-A. Tokheim, and B. M. E. Moldestad, "Investigation of bubbling behavior in deep fluidized beds at different gas velocities using electrical capacitance tomography," *Ind. Eng. Chem. Res.*, vol. 58, no. 5, pp. 2084–2098, Feb. 2019.

[4] Q. Wang, M. Wang, K. Wei, and C. Qiu, "Visualization of gas–oil–water flow in horizontal pipeline using dual-modality electrical tomographic systems," *IEEE Sensors J.*, vol. 17, no. 24, pp. 8146–8156, Dec. 2017.

[5] A. Azzi, H. Bouyahiaoui, A. S. Berrouk, A. Hunt, and I. S. Lowndes, "Investigation of fluidized bed behaviour using electrical capacitance tomography," *Can. J. Chem. Eng.*, vol. 98, no. 8, pp. 1835–1848, Aug. 2020.

[6] L. Ma, D. McCann, and A. Hunt, "Combining magnetic induction tomography and electromagnetic velocity tomography for water continuous multiphase flows," *IEEE Sensors J.*, vol. 17, no. 24, pp. 8271–8281, Dec. 2017.

[7] R. K. Rasel, C. E. Zuccarelli, Q. M. Marashdeh, L.-S. Fan, and F. L. Teixeira, "Toward multiphase flow decomposition based on electrical capacitance tomography sensors," *IEEE Sensors J.*, vol. 17, no. 24, pp. 8027–8036, Dec. 2017.

[8] Q. Marashdeh, "Multi-phase flow decomposition using electrical capacitance volume tomography, sensors," U.S. Patent 16 597 260, Feb. 6, 2020.

[9] N. Li, L. Wang, J. Jia, and Y. Yang, "A novel method for the image quality improvement of ultrasonic tomography," *IEEE Trans. Instrum. Meas.*, vol. 70, Aug. 2021, Art. no. 5000810.

[10] S. Langener, M. Vogt, H. Ermert, and T. Musch, "A real-time ultrasound process tomography system using a reflection-mode reconstruction technique," *Flow Meas. Instrum.*, vol. 53, pp. 107–115, Mar. 2017. [Online]. Available: [Online]. Available: http: //www.sciencedirect.com/science/article/pii/S0955598616300346

[11] G. Liang, S. Ren, S. Zhao, and F. Dong, "A Lagrange-newton method for eit/ut dual-modality image reconstruction," *Sensors*, vol. 19, pp. 1966–1984, 2019.

[12] S. Aumann, S. Donner, J. Fischer, and F. Müller, *Optical Coherence Tomography (OCT): Principle and Technical Realization*. Cham, Switzerland: Springer, 2019, pp. 59–85, doi: 10.1007/978-3-030-16638-0_3.

[13] P. Faia, R. Silva, M. G. Rasteiro, and F. Garcia, "Electrical tomography: A review of configurations, and application to fibre flow suspensions characterisation," *Appl. Sci.*, vol. 10, no. 7, p. 2355, Mar. 2020.

[14] T. A. Khan and S. H. Ling, "Review on electrical impedance tomography: Artificial intelligence methods and its applications," *Algorithms*, vol. 12, no. 5, p. 88, Apr. 2019.

[15] C. Tan, J. Zhao, and F. Dong, "Gas–water two-phase flow characterization with electrical resistance tomography and multivariate multiscale entropy analysis," *ISA Trans.*, vol. 55, pp. 241–249, Mar. 2015, doi: 10.1016/j.isatra.2014.09.010.

[16] F. Li, C. Tan, and F. Dong, "Electrical resistance tomography image reconstruction with densely connected convolutional neural network," *IEEE Trans. Instrum. Meas.*, vol. 70, pp. 1–11, Jul. 2021, Art. no. 4500811.

[17] Y. Fu, C. Tan, and F. Dong, "Analysis of response for magnetic induction tomography with internal source," *Measurement*, vol. 78, pp. 260–277, Jan. 2016.

[18] F. Li, J. F. P. J. Abascal, M. Desco, and M. Soleimani, "Total variation regularization with split bregman-based method in magnetic induction tomography using experimental data," *IEEE Sensors J.*, vol. 17, no. 4, pp. 976–985, Feb. 2017.

[19] Y. Fan and L. Ying, "Solving electrical impedance tomography with deep learning," *J. Comput. Phys.*, vol. 404, Mar. 2020, Art. no. 109119.

[20] J. Kryszyn, P. Wróblewski, M. Stosio, D. Wanta, T. Olszewski, and W. T. Smolik, "Architecture of EVT4 data acquisition system for electrical capacitance tomography," *Measurement*, vol. 101, pp. 28–39, Apr. 2017, doi: 10.1016/j.measurement.2017.01.020.

[21] Q. Guo, X. Li, B. Hou, G. Mariethoz, M. Ye, W. Yang, and Z. Liu, "A novel image reconstruction strategy for ECT: Combining two algorithms with a graph cut method," *IEEE Trans. Instrum. Meas.*, vol. 69, no. 3, pp. 804–814, Mar. 2020.

[22] H. Zhu, J. Sun, L. Xu, W. Tian, and S. Sun, "Permittivity reconstruction in electrical capacitance tomography based on visual representation of deep neural network," *IEEE Sensors J.*, vol. 20, no. 9, pp. 4803–4815, May 2020.

[23] Y. Kang, S. Liu, and J. Liu, "Image reconstruction algorithm for electrical capacitance tomography based on data correlation analysis," *Flow Meas. Instrum.*, vol. 62, pp. 113–122, Aug. 2018.

[24] W. Deabes and H. H. Amin, "Image reconstruction algorithm based on PSO-tuned fuzzy inference system for electrical capacitance tomography," *IEEE Access*, vol. 8, pp. 191875–191887, 2020.

[25] Q. Marashdeh, L.-S. Fan, and R. Williams, "Electrical capacitance, electrical resistance, and positron emission tomography techniques and their applications in multi-phase flow systems," *Adv. Chem. Eng.*, vol. 37, pp. 179–222, Dec. 2009.

[26] W. Deabes, A. Sheta, K. E. Bouazza, and M. Abdelrahman, "Application of electrical capacitance tomography for imaging conductive materials in industrial processes," *J. Sensors*, vol. 2019, pp. 1–22, Dec. 2019. [Online]. Available: https://www.hindawi.com/journals/js/2019/4208349/

[27] M. B. Haddadi and R. Maddahian, "A new algorithm for image reconstruction of electrical capacitance tomography based on inverse heat conduction problems," *IEEE Sensors J.*, vol. 16, no. 6, pp. 1786–1794, Mar. 2016.

[28] R. Kumar, S. kumar, and A. Sengupta, "A review: Electrical impedance tomography system and its application," *J. Control Instrum.*, vol. 7, no. 2, pp. 14–22, 2019.

[29] S. Abbasian and R. Maddahian, "Image reconstruction of electrical capacitance tomography using the dynamic mesh and changing physical properties methods," *Meas. Sci. Technol.*, vol. 31, no. 1, Jan. 2020, Art. no. 015402.

[30] H. Guo, S. Liu, H. Cheng, S. Sun, J. Ding, and H. Guo, "Iterative computational imaging method for flow pattern reconstruction based on electrical capacitance tomography," *Chem. Eng. Sci.*, vol. 214, Mar. 2020, Art. no. 115432.

[31] B. I. Andia, K. D. Sauer, and C. A. Bouman, "Nonlinear backprojection for tomographic reconstruction," *IEEE Trans. Nucl. Sci.*, vol. 49, no. 1, pp. 61–68, Feb. 2002. [Online]. Available: http://ieeexplore.ieee.org/articleDetails.jsp?arnumber=998682

[32] T. Tirer and R. Giryes, "Back-projection based fidelity term for ill-posed linear inverse problems," *IEEE Trans. Image Process.*, vol. 29, pp. 6164–6179, Dec. 2020.

[33] Z. Cui, Q. Wang, Q. Xue, W. Fan, L. Zhang, Z. Cao, B. Sun, and H. Wang, "A review on image reconstruction algorithms for electrical capacitance/resistance tomography," *Sensor Rev.*, vol. 36, no. 4, pp. 429–445, 2016.

[34] M. Neumayer, H. Zangl, D. Watzenig, and A. Fuchs, "Current reconstruction algorithms in electrical capacitance tomography," *New Develop. Appl. Sens. Technol.*, vol. 83, pp. 65–106, Dec. 2011.

[35] M. A. Abdelrahman, A. Gupta, and W. A. Deabes, "A feature-based solution to forward problem in electrical capacitance tomography of conductive materials," *IEEE Trans. Instrum. Meas.*, vol. 60, no. 2, pp. 430–441, Feb. 2011.

[36] I. Saksen, "A review of reconstruction techniques for capacitance tomography," *Meas. Sci. Technol.*, vol. 7, no. 3, pp. 325–337, Mar. 1996. [Online]. Available: http://stacks.iop.org/0957-0233/7/i=3/a=013?key=crossref.231a7f284f65ff56d86b1ae1f0e5a073
[37] M. Soleimani, C. N. Mitchell, R. Banasiak, R. Wajman, and A. Adler, "Four-dimensional electrical capacitance tomography imaging using experimental data," *Prog. Electromagn. Res.*, vol. 90, pp. 171–186, Dec. 2009.
[38] H. Yan, Y. H. Sun, Y. F. Wang, and Y. G. Zhou, "Comparisons of three modelling methods for the forward problem in three-dimensional electrical capacitance tomography," *IET Sci., Meas. Technol.*, vol. 9, no. 5, pp. 615–620, Aug. 2015.
[39] J. Lei, S. Liu, and X. Y. Wang, "Dynamic inversion in electrical capacitance tomography using the ensemble Kalman filter," *IET Sci., Meas. Technol.*, vol. 6, no. 2, pp. 63–77, Mar. 2012. [Online]. Available: http://digital-library.theiet.org/content/journals/10.1049/iet-smt.2011.0193
[40] G. Evensen, "Sequential data assimilation with a nonlinear quasi-geostrophic model using Monte Carlo methods to forecast error statistics," *J. Geophys. Res.*, vol. 99, no. 5, pp. 10143–10162, 1994. [Online]. Available: https://agupubs.onlinelibrary.wiley.com/doi/abs/10.1029/94JC00572
[41] G. Evensen, "The ensemble Kalman filter: Theoretical formulation and practical implementation," *Ocean Dyn.*, vol. 53, no. 4, pp. 343–367, Nov. 2003.
[42] M. Eknes and G. Evensen, "An ensemble Kalman filter with a 1-D marine ecosystem model," *J. Mar. Syst.*, vol. 36, nos. 1–2, pp. 75–100, Jul. 2002.
[43] J. I. Allen, M. Eknes, and G. Evensen, "An ensemble Kalman filter with a complex marine ecosystem model: Hindcasting phytoplankton in the cretan sea," *Ann. Geophys.*, vol. 20, pp. 1–13, Dec. 2002.
[44] E. Geir, *Data Assimilation: Ensemble Kalman 'Filter*. Cham, Switzerland: Springer, 2009.
[45] T. LLC. (Aug. 2020). *Electrical Capacitance Volume Tomography*. [Online]. Available: https://www.tech4imaging.com/electrical-capacitance-volume-tomography/

WAEL DEABES received the B.S. and M.S. degrees in computer and electrical engineering from Mansoura University, Mansoura, Egypt, in 1999 and 2003, respectively, and the Ph.D. degree in computer engineering from Tennessee Technological University, USA, in 2010. He is currently working as an Associate Professor with the Computer Science Department, Umm Al-Qura University, Saudi Arabia. He has published one book, more than 40 articles in international journals and conferences, and holds one patent. His areas of expertise include electrical tomography, artificial intelligence, control systems, the Internet of Things (IoT), smart cities, and embedded systems. He served as a reviewer for several journals and conferences, including ISA, IEEE SENSORS JOURNAL, and IEEE TRANSACTIONS ON IMAGE PROCESSING. He served as a PI and Co-PI for several funded grants from the King Abdulaziz City for Science and Technology and other international fund agencies.

KHEIR EDDINE BOUAZZA received the B.Eng. degree in computer science from the University of Oran, Algeria, in 1998, and the M.Sc. degree in automatic control and digital signal processing and the Ph.D. degree in automatic control from the University of Lorraine, France, in 2000 and 2004, respectively. From 2004 to 2005, he was a Research Associate (ATER) with the Department of Computer Engineering, IUT de Longwy, University of Lorraine. From 2005 to 2010, he was an Assistant Professor and Associate Professor with the University of Oran. He is currently an Associate Professor with the University of Umm Al-Qura (UQU), Saudi Arabia. His main research interests include networked control systems, intelligent control systems, non-linear control and estimation, time delay systems, digital signal processing, and wireless sensor networks.